Multi-beam coherent Fourier scatterometry

Soman, S.; Horsten, R.C.; Scholte, T.C.; Pereira, S.F.

Important note
To cite this publication, please use the final published version (if applicable).
Please check the document version above.

PAPER • OPEN ACCESS

Multi-beam coherent Fourier scatterometry

To cite this article: S Soman *et al* 2024 *Meas. Sci. Technol.* **35** 075905

View the article online for updates and enhancements.

Multi-beam coherent Fourier scatterometry

S Soman*[ORCID], R C Horsten, T Scholte and S F Pereira

Department of Imaging Physics, Delft University of Technology, Lorentzweg 1, 2628 CJ Delft, The Netherlands

E-mail: s.soman@tudelft.nl

CrossMark

Abstract

Inspection of surface and nanostructure imperfections play an important role in high-throughput manufacturing across various industries. This paper introduces a novel, parallelised version of the metrology and inspection technique: Coherent Fourier scatterometry (CFS). The proposed strategy employs parallelisation with multiple probes, facilitated by a diffraction grating generating multiple optical beams and detection using an array of split detectors. The article details the optical setup, design considerations, and presents results, including independent detection verification, calibration curves for different beams, and a data stitching process for composite scans. The study concludes with discussions on the system's limitations and potential avenues for future development, emphasizing the significance of enhancing scanning speed for the widespread adoption of CFS as a commercial metrology tool.

Keywords: scatterometry, parallel, metrology

1. Introduction

In the last few decades, there has been an increased push towards making devices with smaller features and different materials across different industries. Industries like semiconductor manufacturing rely heavily on metrology and inspection tools to optimise their fabrication process, ensuring device performance and power efficiency [1, 2]. Other industries like biomedicine, security, power electronics and photonics have also seen a growing requirement for both in-line and off-line metrology tools [3–6]. In a landscape marked by swift innovation and production cycles, fast metrology tools are vital to maintaining high-throughput manufacturing.

Traditional high-end measurement techniques like electron microscopy (SEM and TEM) or atomic force microscopy (AFM) provide high spatial and axial resolution but have limitations including slow data collection, potential sample damage and dependence on stringent measurement conditions, making them less ideal for in-line measurements. Scatterometry, a manufacturing metrology workhorse, is a non-imaging, model-based, optical technique that allows sub-nanometer measurements of isolated or periodic structures, optical constants, material properties or roughness [2, 7–9]. Coherent Fourier scatterometry (CFS) is an advanced scatterometry technique which captures the scattered field from multiple angles incident on the sample plane using a focused spot [10]. The focused spot is scanned across the sample surface and the signal from each position is collected in the far-field plane. CFS has been shown to have high sensitivity but is inherently limited by the scanning speed of the setup. It is crucial to improve the scanning speed of the technique to facilitate its wider adoption as a commercial metrology tool.

In this paper, we propose a parallelisation strategy employing multiple probes to reduce total scan time. Similar strategies have been employed in other domains such as optical data storage, SEM and confocal microscopy where throughput is generally limited by the scanning time [11–15]. Here, we use a

---

* Author to whom any correspondence should be addressed.

diffraction grating to generate multiple optical beams and an array of split detectors for detection.

The article is organised as follows: in section 2, we describe the optical setup and explain the design considerations. Section 3 details the results, divided into four subsections. First, we verify that the detection is independent across the beams. Then, we show the calibration curves for the different beams for known scatterers. Thereafter, we briefly describe the process of data stitching to generate a composite scan. Finally, we show an example of possible limitations of the system using transparent samples. In section 4, we present the discussions and possible outlook.

2. Experimental setup

Figure 1(a) shows the experimental setup of the multi-beam CFS. Light from a HeNe ($\lambda = 633$ nm) laser is collimated and magnified using lenses L1 and L2 in a telescopic arrangement. A 1D beam-splitter (TS-280-P-Y-A_1D, HoloOR) is then used to split the incident beam into three beams of similar intensities. The power and angular separation from the optical axis for each beam is given in table 1.

The three beams are then relayed to the back focal plane of the microscope objective. The relay consists of a scan lens (L3, $f = 39$ mm)—tube lens (L4, $f = 165$ mm) pair in a telescopic arrangement. The scan lens is used to flatten the focal plane curvature for the off-axis beams before the objective. This ensures that the beams after the objective have the best focus in the same plane. The objective (Leica, N PLAN L 20x/0,40) used in the setup has a numerical aperture (NA) of 0.4. The beams, after scattering from the sample, are collected in reflection with the same objective. They are relayed from the back focal plane of the objective to the detector using the lenses L5 and a microlens array (MLA) in yet another telescopic arrangement. The microlens array (MLA1M1, Thorlabs) collimates each beam separately before being incident on the detector. The off-axis beams suffer from higher optical aberrations compared to the on-axis beam. Defocus and astigmatic aberrations, in particular, can cause a reduction in the signal peak–peak voltage measured at the detector. Thus it is important to have optical elements that can reduce these aberrations for the beams at higher angles. The coefficients for the defocus and astigmatic aberrations for each beam are measured at the back focal plane of the objective and are shown in table 1.

The detector consists of an array of Si photodiodes (S4111-16R, Hamamatsu) with every two photodiodes working as a split detector. The light incident on each diode generates a photocurrent and the split detector signal is generated by subtracting one from the other. The microlens array was chosen such that the separation between two micro lenses was equal to the separation between two split detector pairs on the the detector. This ensures that each beam can be made to be incident exactly in the middle of two photodiodes. A non-zero signal is generated only when there is an asymmetry in the field incident of

Table 1. Optical properties of the three beams. The wavefront aberrations were measured using a Shack-Hartmann wavefront sensor.

	Beam 1	Beam 2	Beam 3
Power (uW)	29	33.8	29.6
Angle	$-1.22°$	0	$1.22°$
Defocus (λ)	-0.0072	-0.0081	0.0059
Ast 0° (λ)	0.0195	0.0283	0.0197
Ast 45° (λ)	-0.0211	-0.0023	-0.0223

the split detector. This helps to eliminate common mode signals generated from surface reflections or other spurious ghost reflections. The difference signal generated from each pair of photodiodes is amplified, sampled using an ADC and represented as a 2D data using the position feedback signal of the scan stage measured synchronously with the detector signal. The 2D mechanical scanning is performed by raster scanning the sample in the x and y-directions using a piezo stage, P-625.2 CD (see figure 1(b)). An additional z-piezo, S-316.10H is used to position the sample in the focal plane of the objective. A camera is also added to locate areas of interest on the sample.

A schematic of the detection module is shown in figure 1(a). Figure 2 shows the typical signal generated from one beam when scanning across a hole etched on a Si wafer. The signal was obtained by scanning the sample at a speed of 0.67 mm s^{-1}. It consists of a positive and negative peak corresponding to the asymmetries generated in the far-field along the direction of the scan. The magnitude of the peak value with respect to the baseline is proportional to the size of the scatterer. The minimum detectable size is determined by the signal-to-noise ratio of the signal generated from the scanning and the noise floor of the detector. A brief description of the noise sources in the system is presented in appendix B.

2.1. Design considerations

As compared to a single beam CFS that uses an on-axis beam to generate a focused spot, the multi-beam design has more parameters that can influence the output signal. Here, we discuss two such parameters in detail, namely, the interfocal separation and the beam separation at the detector plane.

2.1.1. Interfocal separation. The spot separation at the focal plane is controlled by the angular separation of the beams, demagnification of the relay lens and the NA of the objective. A focused spot on the surface is not limited to the spot diameter defined by the distance to the first minima of the Airy spot [16]. Theoretically, it extends infinitely and can interact with a scatterer at infinity. However, for practical purposes, we define the effective spot diameter to be twice the minimum distance from the center of the spot to the center of a scattering object, such that, the signal generated by the interaction
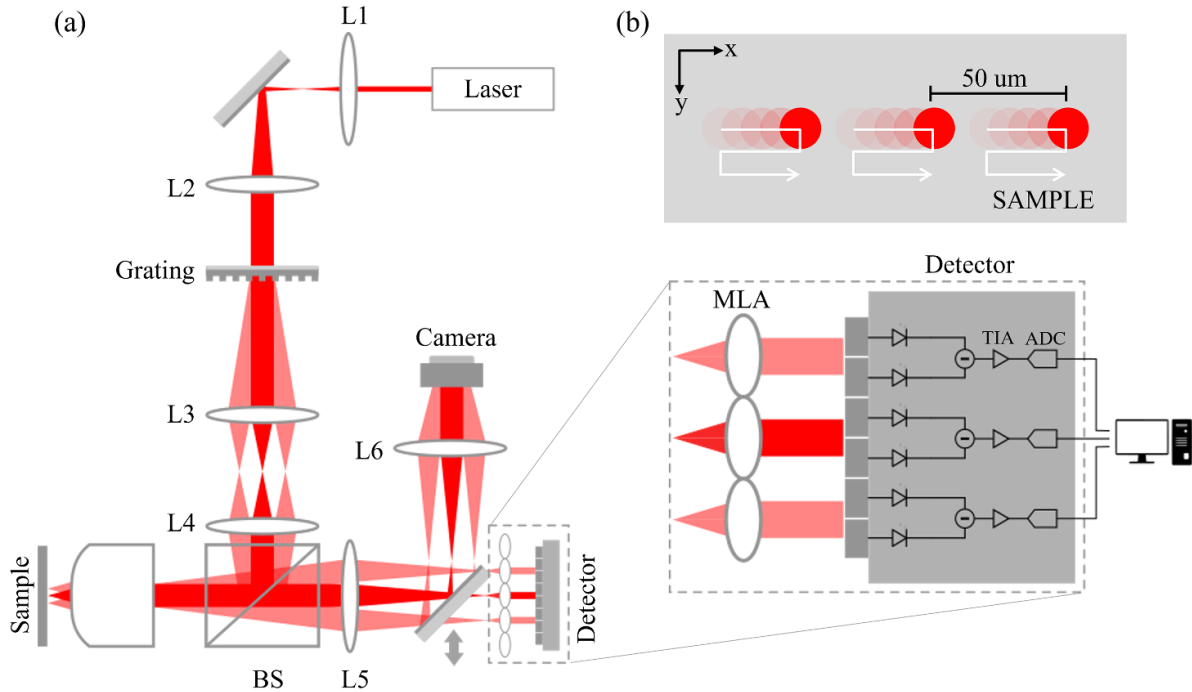
Figure 1. (a) Schematic diagram of the setup. Objective of 0.4 NA, camera for locating features, grating to generate three beams, MLA microlens array to collimate beams individually before the detector and split detector array for detecting each beam separately, L1—5 mm, L2—250 mm, L3 (scan lens)—39 mm, L4 (tube lens)—165 mm, L5—410 mm, L6—200 mm. (b) Raster scan schematic using the three beams.
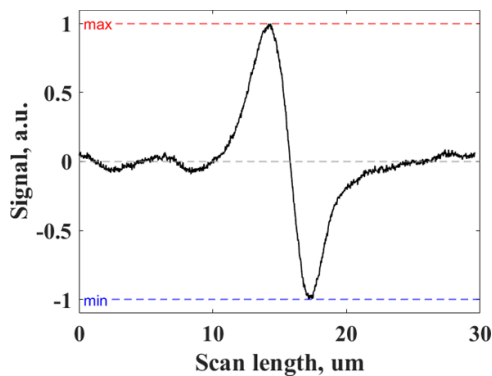

Figure 2. Typical output signal measured using a single beam CFS. The signal measured is from a scan of a 400 nm PSL particle on a Si wafer using an objective of 0.4 NA at 633 nm wavelength. The scan speed is 0.67 mm s^{-1}. The signal strength is quantified as mean(max, |min|).

of the spot with the object is higher than the noise level of the detector. Using the biggest scatterer size in the measurement, a 1000 nm etched hole in Silicon, we define the effective diameter of the focused spot to be 1.6 times the focused spot diameter. A detailed derivation of this calculation is shown in appendix B. For an NA of 0.4 at 633 nm wavelength the effective spot diameter is then 2.954 μm. To ensure that there is no detectable cross-talk between the two adjacent beams, we set the interfocal separation between them to be greater than this value by a safety factor of 10. The probability of cross-talk

decreases as the separation increases but larger separations can lead to higher optical aberrations for the beams at higher angles.

The final factor that needs to be considered is the sample thickness (in the case of transparent samples or samples with transparent layers). The influence of the sample thickness on cross-talk is negligible if the thickness is less than the depth of focus of the spot [17]. The depth of focus in this case is calculated to be 3.95 μm. For measurement surfaces with high reflectivity like metals or Si, this should pose no problem. However, for transparent samples with lower reflectivity, this factor should additionally be taken into account for optimising the interfocal separation. One solution would be to increase the physical separation between the detectors or to add a pinhole array before micro-lens array.

2.1.2. Beam separation at the detector array. At the detector, each beam is incident exactly in the middle of two photodiodes such that when the beam is symmetric, the output signal is zero. The same target can result in different output signals depending on the offset of the beam with respect to this balanced position. Figure 3 shows the change in output signal when the beam is offset by different amounts with respect to the split-detector. The output signals are numerically calculated for a hole with a diameter of 400 nm and depth 150 nm etched in a Si substrate illuminated with a focus spot of 0.4 NA at a wavelength of 633 nm using the commercial
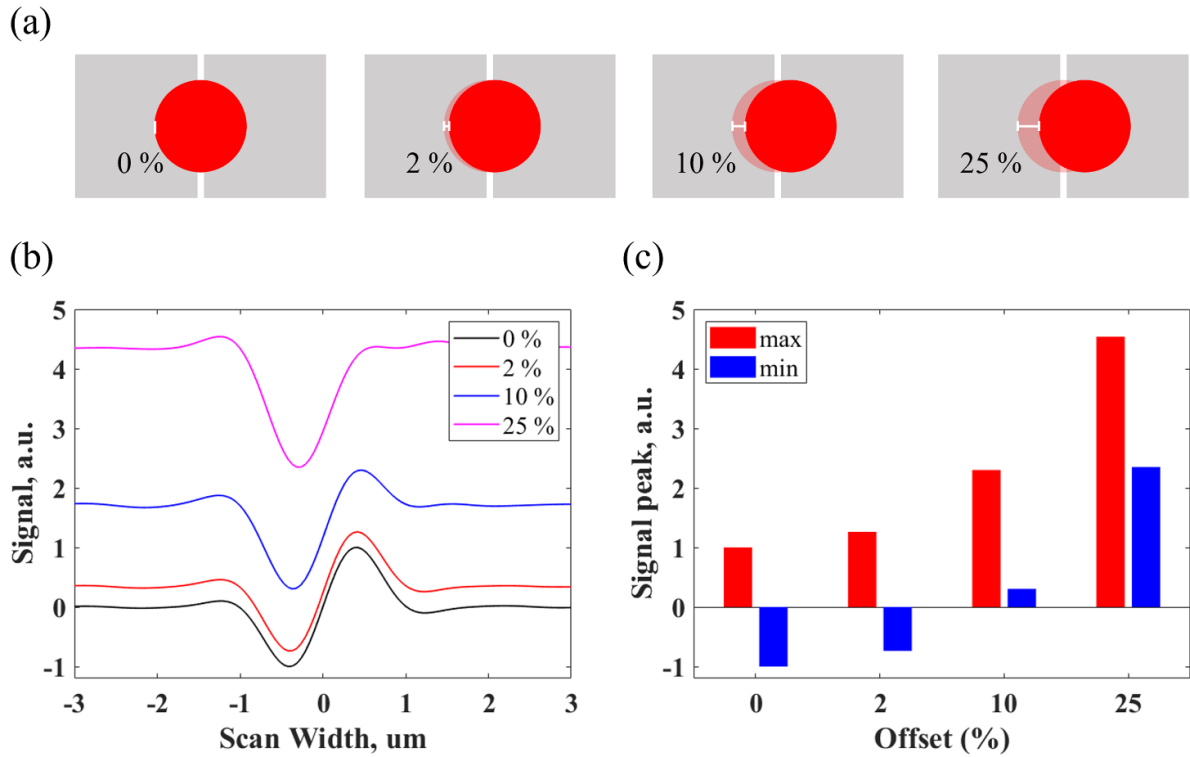
Figure 3. Scans with different beam offsets at the detector. (a) Schematic of different beam offsets at the detector. (b) Scans with different detector offset. (c) The absolute values of the maximum and minimum values of the signals. The signals are generated by simulating different offsets as a percentage of the beam diameter (detector size $\gg$ beam diameter). The signal was simulated for a scan of a Si wafer with an etched hole of 400 nm diameter and 150 nm depth.
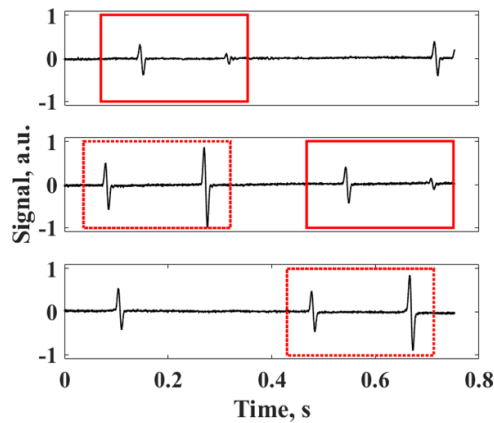

Figure 4. Differential readout signal from the detector array. The beams are arranged horizontally and scanned over PSL particles. The separation between two adjacent spots is 50 μm. The rectangles show repeating signals as adjacent beams scan the same region. The scan range for each beam is 100 μm. The signal is sampled at 50 kHz sampling rate.

solver, Lumerical. Offset errors can lead to misinterpretation of the collected data and can negatively impact the quality of the measurement. Thus, it is important that the beam separation at the detector matches the pitch of the detector array to within a few micrometers. This places rather strict requirements on the alignment tolerances of the optical elements but enables identical output signals for all beams when scanning the same target. The condition can be relaxed if the offset is calibrated in advance and taken into account during the post-processing after acquisition.

3. Results

3.1. Independent detection

Initial experiments were performed to verify that the detection was independent across the beams, i.e. when one beam interacts with a target, the other two beams are not affected. A snapshot of the signal from the three beams is shown in figure 4. The beams are arranged horizontally and allowed to scan over the surface of a Si wafer containing spherical
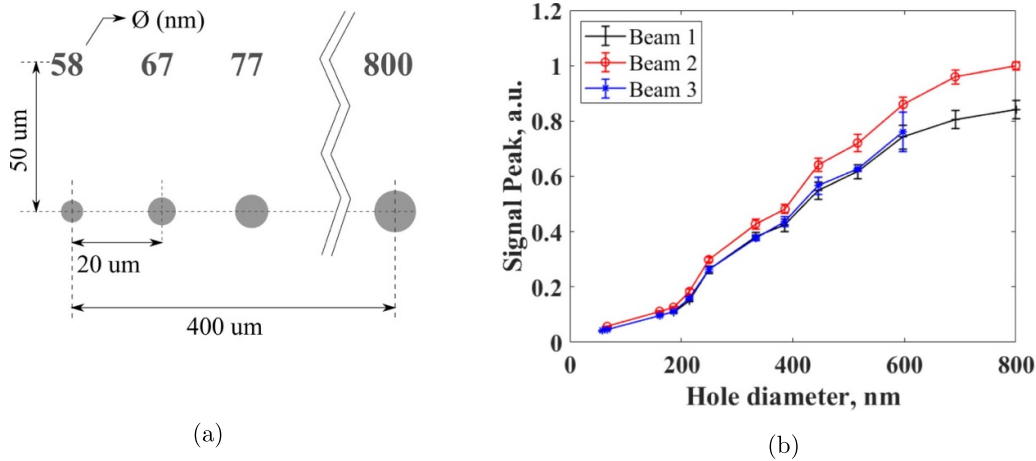
(a)

(b)

Figure 5. (a) Sample schematic. The sample consists of an array of holes of diameters distributed exponentially from 50 to 800 nm etched on a Si wafer. The etch depth is 150 nm. (b) Calibration curve for different beams. Scan is performed using 0.4 NA objective with 633 nm wavelength.

polystyrene latex (PSL) particles. The scan range is 100 um, scanned at a speed of 0.33 mm s^{-1} with a sampling rate of 50 kHz. The scan range is larger than the separation between the beams and the signals from the overlapping areas can be seen repeating across multiple beams. It is also evident that there is no discernible cross-talk between the beams.

3.2. Calibration

The setup was used to measure the signal from a sample of known characteristics for validation of the parallel scanning strategy. The measurement sample consists of an array of holes etched into a Si substrate. The hole diameters are exponentially distributed from 50 to 800 nm. The etch depth for all the structures is 150 nm. The separation between individual structures is 20 μm. A schematic of the sample is shown in figure 5(a). The signal strength corresponding to each hole is defined as the average of the absolute value of the maximum and minimum peaks of the signal. The scans were done at a speed of 0.3 mm s^{-1} and sampled at 50 kHz sampling rate. Calibration measurements in figure 5(b) show that the overall trend is identical across the three beams but is scaled due to the power difference across the three beams.

3.3. Data stitching

Tiling scans from the different beams is implemented using phase correlation algorithm [18]. The algorithm used for the data processing and stitching is included in appendix C. If the exact separation between the beams is unknown, it is useful to have a small amount of overlap to enable stitching and maintaining full area coverage. An example of the separate scans from each beam and the composite stitched image is shown in figure 6. The sample consists of a Si wafer with etched structures. The scan area per beam is 100 um × 100 um. The separation between the lines is 200 nm. The scan speed for the fast axis is 0.33 mm s^{-1}. The fast axis is along the *x*-direction.

The sampling rate is 50 kHz. The minimum overlap between scans from individual beams for stitching this particular scan was 15%.

The algorithm, while useful in case of sparse samples, needs further modification if the scan area consists of periodic structures like gratings.

4. Discussions

In summary, we presented a parallelised coherent Fourier scatterometry setup using multiple beams. The detection was shown to be independent across the beams for non-transparent samples. The output signal was measured to be identical for all the beams barring any power differences. The geometrical parameters of the scattering structures can be retrieved using suitable calibration curves. A data stitching algorithm to generate a composite image from the individual scans has also been implemented. A possible limitation of the multi-beam setup is in the case of transparent samples or samples with thin layers due to possible multiple reflections that can cause crosstalk.. However, this can be avoided by increasing the distance between the spots on the sample or by reducing the reflection from the back surface of the sample.

The system can be scaled to use a higher number of beams generated using a 2D beam-splitter, microlens array, or an array of laser diodes combined with a 2D microlens array and split detector array for detection. The maximum number of spots would be limited by the higher field curvature and distortion for the beams at larger angles, equivalent to the field of view in microscopy. Other design variations to overcome this problem would include the use of a high-NA microlens array to generate multiple spots on the sample instead of a single objective and a suitable telescopic system to relay the respective Fourier planes to the detector array.

Electronic complexity increases as the number of probes increases. The current scan speed is limited by the use of piezo-based translation stages. This makes the system in its current
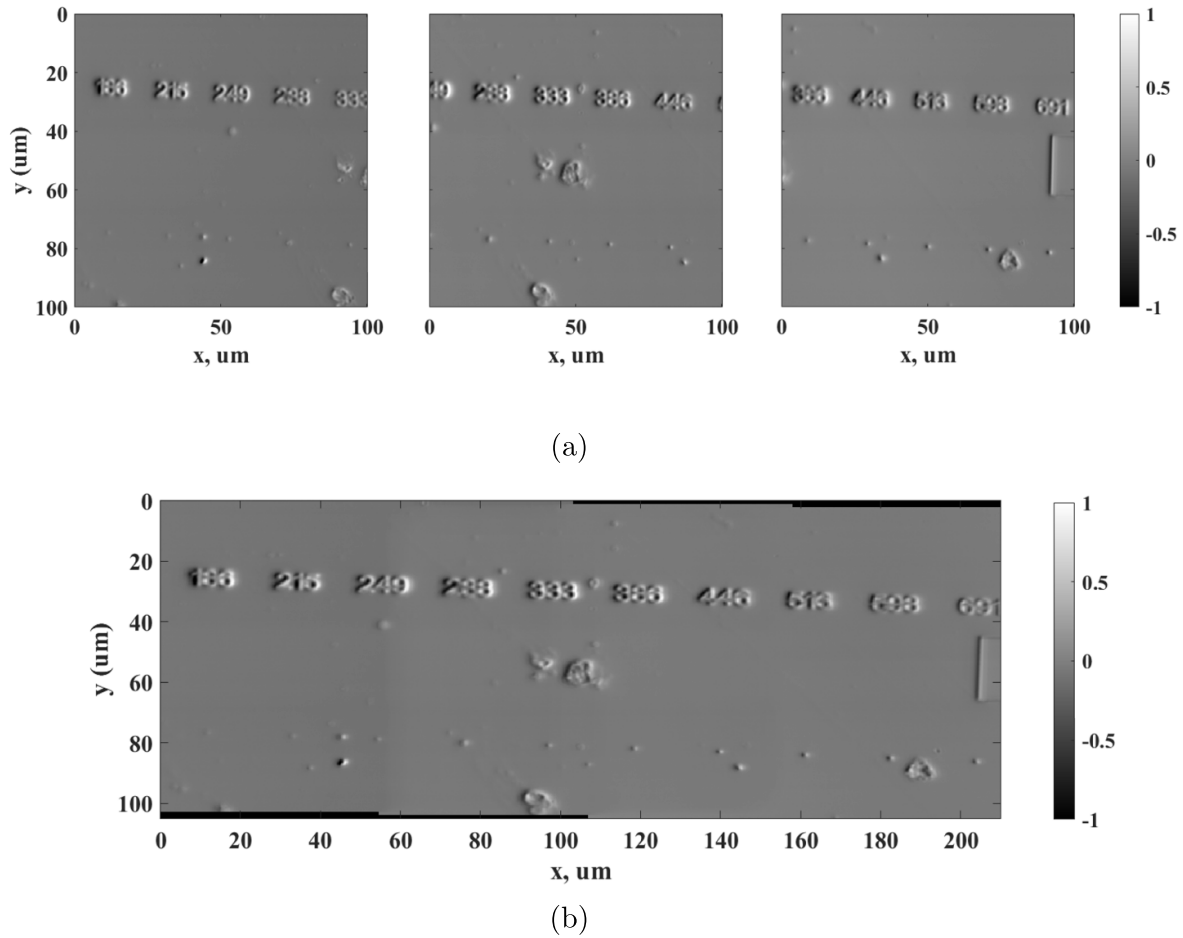
(a)

(b)

Figure 6. (a) The scans from three independent beams before stitching. (b) The composite scan after stitching using phase correlation algorithm. The scan parameters for each beam are: scan area—$100\,\mu m \times 100\,\mu m$, scan speed (fast axis)—0.33 mm s^{-1}, separation between lines in the y-direction—200 nm, sampling rate—50 kHz.

design a few orders of magnitude slower than other commercial surface metrology tools such as dark-field microscopy or white-light interferometry. For even faster scan speeds, other forms of scanning such as using a galvo mirror, rotating polygon mirror or acousto-optic deflectors in place of the piezo-scanners can be investigated. They could also be combined with the multiple beam scheme we presented here.

Since CFS is a non-imaging technique based on a-priori information of the sample, the isolated minimum structure size that can be measured is limited by the measurement noise. The resolution of the system is comparable to other optical scanning techniques such as confocal microscopy. However, since we use differential detection scheme common mode measurement noise are eliminated and larger signal gain can be reached. The use of photo-diodes also means that the detection bandwidth could be pushed to accommodate faster scan speeds while maintaining a low noise floor.

Data availability statement

The data cannot be made publicly available upon publication because no suitable repository exists for hosting data in this field of study. The data that support the findings of this study are available upon reasonable request from the authors.

Appendix A. Setup and alignment

Figure A1 shows a picture of the physical setup on the optical table. The list of components with their properties is shown in table A1. The CFS setup is constructed using different 4f
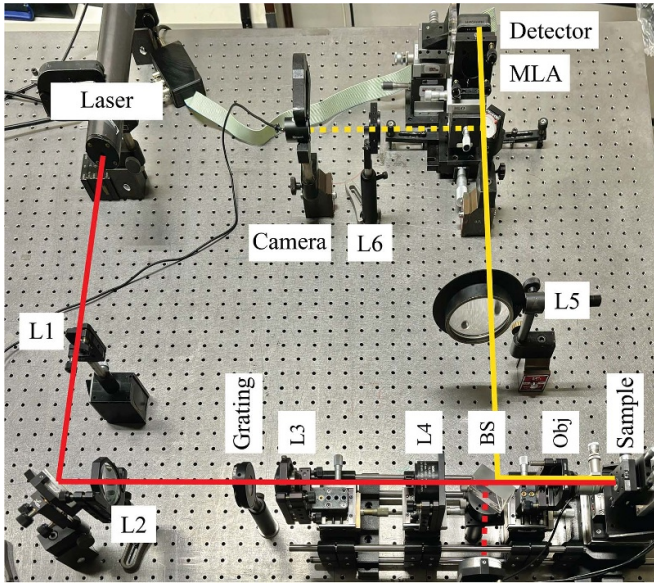
Figure A1. A photo of the setup on the optical table.

Table A1. List of components.

Laser	Wavelength (nm)
HeNe	633

Lens	Focal length (mm)
L1	5
L2	250
L3	39 (LSM03-VIS, Thorlabs)
L4	165 (TTL165-A, Thorlabs)
L5	410
L6	200
MLA	4 (MLA1M1, Thorlabs)
Objective	Leica, N PLAN L 20x/0,40
Detector	S4111-16R, Hamamatsu
Camera	Microsoft LifeCam Cinema
Grating	TS-280-P-Y-A 1D, HoloOR

Stage	Model
Piezo-*x*	P-625.2 CD
Piezo-*y*	P-625.2 CD
Piezo-*z*	S-316.10H

systems as the building blocks. The first 4f system formed by lenses L1 and L2 is used to collimate and magnify the light from the laser. The second block formed by lenses L3 and L4 serves to both relay the grating to the pupil plane of the objective and flatten the field curvature for the off-axis beams. The final block formed by lens L5 and MLA both relays and separately collimates the beams onto the detector. In all cases, the separation between the lenses in each pair has to be equal to the sum of the focal length of each lens for it to relay the beam without distorting its spatial distribution. This is verified using a shear plate to check for the collimation after each pair. The position of the lens L5 and the distance between the grating and lens L3 is quite important to ensure that the separation of the beams at the detector is exactly 2 mm.

Appendix B. Area of influence of a spot

The minimum detectable signal is limited by system noise. The most important sources of noise in the total system are the shot noise, electronic noise, quantisation noise and surface roughness (media noise). In our case, the output detector signal has a range of $2V_{pp}$ and a noise floor of 35.9 mV$_{pp}$ including both the electronic and surface noises. The dynamic range of the system can then be calculated to be around 35 dB. To calculate the area of influence of a spot, we first consider the signal generated when the spot scans a small scatterer in case of an ideal system i.e. no optical aberrations, electronic noise or surface roughness. The process was simulated using rigorous 3D electromagnetic solver, Lumerical. The simulation domain consists of a silicon substrate ($n = 3.882 + i0.019$) with an etched hole of 1 µm diameter and 150 nm depth. The input source is *x*-polarised, i.e polarised in the direction in the direction of the scan, 0.4 NA focused spot at 633 nm wavelength. The FDTD simulations in Lumerical allows the user to import custom input field [19]. The focus field was calculated analytically using the formalism as described in Assafrão [20]. The total FDTD simulation domain has a span of $15 \times 15 \times 0.7$ µm. The near to far-field projection is calculated using the in-built far field projection functions [21].

To calculate the area of influence of a spot, we make the assumption that the size of the biggest scatterer we measure is 1 µm. We define the effective spot size to be the maximum separation between the point scatterer and the center of the focused spot such that the signal generated is above twice the noise floor of the detector. The separation is different in *x* and *y*-directions because the difference signal is calculated in the direction of the scan namely along the *x*-axis. It can be calculated from figure B1 that effective spot radius for our system is 1.596 µm i.e. 1.65 times the radius of the focused spot defined to be the distance from the center of the spot to the first minima, along the *x*-axis and 0.818 µm along the *y*-axis.
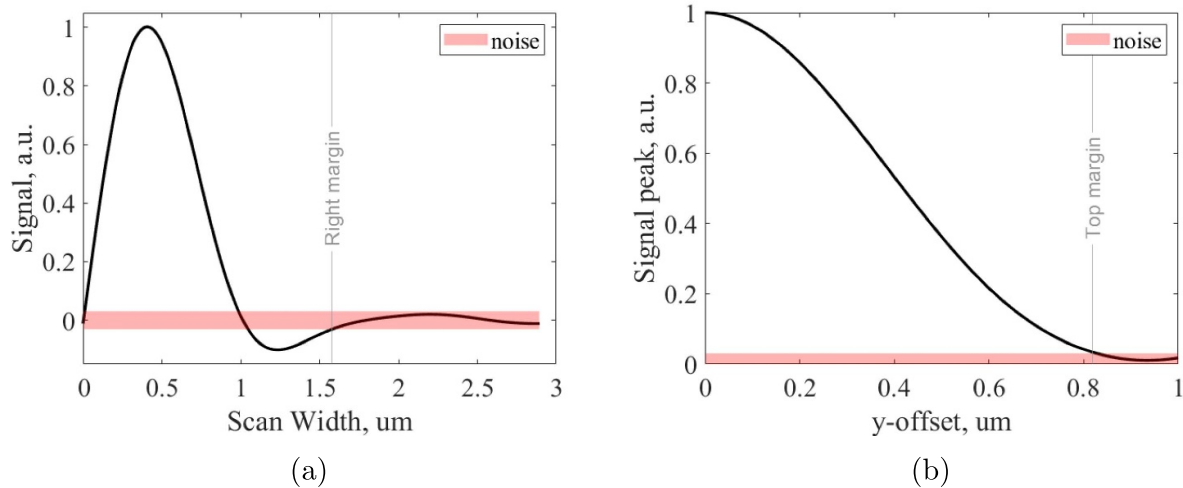
Figure B1. Signal simulated for a focused spot of 0.4 NA and 633 nm wavelength scanning a etched hole of 1000 nm diameter and 150 nm etch depth. (a) The signal from a scan in *x*-direction passing through the middle of the particle, (b) signal peak for scans in *x*-direction but with different shifts in the *y*-direction with respect to the particle. The red bar represents the noise floor of the system.

Algorithm 1. Phase correlation algorithm [18].

Input: I_1, I_2
Output: (x, y): Translation coordinates
1: **procedure** PHASECORRELATION(I_1, I_2)
2: $F_1 \leftarrow \text{fft}(I_1)$ ▷ 2D Fourier transform
3: $F_2 \leftarrow \text{fft}(I_2)$
4: NCC $\leftarrow (F_1.*\bar{F}_2)./\text{abs}(F_1.*\bar{F}_2)$ ▷ Calculate normalised cross-correlation
5: PCM $\leftarrow \text{ifft}(\text{NCC})$ ▷ Calculate phase correlation matrix
6: (x, y) $\leftarrow \text{argmax}(\text{PCM})$
7: **end procedure**

Appendix C. Data stitching

The scans from different beams are stitched using a phase correlation algorithm as shown in algorithm 1. The algorithm calculates the x and y values that one scan needs to be translated with respect to the previous one to have perfect overlap.

ORCID iD

S Soman https://orcid.org/0000-0002-8316-8639

References

[1] IEEE 2022 *International Roadmap for Devices and Systems 2022 Edition—Metrology* (available at: https://irds.ieee.org/editions/2022/irds%E2%84%A2-2022-metrology)
[2] Orji N G *et al* 2018 Metrology for the next generation of semiconductor devices *Nat. Electron.* **1** 532–47
[3] Kim S, Jung U T, Kim S-K, Lee J-H, Soo Choi H S, Kim C-S and Jeong M Y 2015 Nanostructured multifunctional surface with antireflective and antimicrobial characteristics *ACS Appl. Mater. Interfaces* **7** 326–31
[4] Javidi B *et al* 2016 Roadmap on optical security *J. Opt.* **18** 083001
[5] Hatakeyama T, Ichinoseki K, Fukuda K, Higuchi N and Arai K 2008 Evaluation of the quality of commercial silicon carbide wafers by an optical non-destructive inspection technique *J. Cryst. Growth* **310** 988–82
[6] Chen Z and Segev M 2021 Highlighting photonics: looking into the next decade *eLight* **1** 2
[7] Ghafoori M, Bahrenberg L, Glabisch S, Schroeder S, Danylyuk S, Brose S, Stollenwerk J, Juschkin L and Loosen P 2021 Broadband scatterometry at extreme ultraviolet wavelengths for nanograting characterization *Proc. SPIE* **11611** 116112F
[8] Diebold A C, Antonelli A and Keller N 2018 Perspective: optical measurement of feature dimensions and shapes by scatterometry *APL Mater.* **6** 058201
[9] Herrero A F, Scholze F, Dai G and Soltwisch V 2022 Analysis of line-edge roughness using EUV scatterometry *Nanomanuf. Metrol.* **5** 149–58
[10] Roy S, Assafrao A C, Pereira S F and Urbach H P 2014 Coherent Fourier scatterometry for detection of nanometer-sized particles on a planar substrate surface *Opt. Express* **22** 13250–62
[11] Carlin D B, Bednarz J P, Kaiser C J, Connolly J C and Harvey M G 1984 Multichannel optical recording using monolithic arrays of diode lasers *Appl. Opt.* **23** 3994–4000
[12] Ishihara M and Sasaki H 1999 High-speed surface measurement using a non-scanning multiple-beam confocal microscope *Opt. Eng., Bellingham* **38** 1035–40
[13] Tiziani H J and Uhde H-M 1994 Three-dimensional analysis by a microlens-array confocal arrangement *Appl. Opt.* **33** 567–72

[14] Katayama R, Yoshihara K, Yamanaka Y, Tsunekane M, Kubota K and Yoshida K 1989 Multi-beam magneto-optical disk drive for parallel read/write operation *Optical Data Storage* (Optica Publishing Group) p WA3

[15] Eberle A L, Mikula S, Schalek R, Lichtman J, Tate M L K and Zeidler D 2015 High-resolution, high-throughput imaging with a multibeam scanning electron microscope *J. Microsc.* **259** 114–20

[16] Inoué S 2006 *Foundations of Confocal Scanned Imaging in Light Microscopy* (Springer US) pp 1–19

[17] Egner A, Andresen V and Hell S W 2002 Comparison of the axial resolution of practical Nipkow-disk confocal fluorescence microscopy with that of multifocal multiphoton microscopy: theory and experiment *J. Microsc.* **206** 24–32

[18] Preibisch S, Saalfeld S and Tomancak P 2009 Globally optimal stitching of tiled 3D microscopic image acquisitions *Bioinformatics* **25** 1463–5

[19] Ansys Optics 2024 *Far field projections in FDTD overview* (available at: https://optics.ansys.com/hc/en-us/articles/360034914713-far-field-projections-in-fdtd-overview) (Accessed 4 March 2024)

[20] Assafrão A C 2013 On super resolved spots in the near-field regime *PhD Thesis* Technische Universiteit Delft

[21] Ansys Optics 2024 *Import source - Simulation object* (available at: https://optics.ansys.com/hc/en-us/articles/360034383014-import-source-simulation-object) (Accessed 4 March 2024)